Efficient Intraband Hot Carrier Relaxation in the Perovskite Semiconductor $Cs_{1-x}Rb_xSnI_3$ Mediated by Strong Electron-phonon Coupling

M. Monti,[†] S. X. Tao,[‡] M. Staniforth,[†,¶] A. Crocker,[†] E. Griffin,[†] A. Wijesekara,[¶] R. A. Hatton,[¶] and J. Lloyd-Hughes[*,†]

[†]*University of Warwick, Department of Physics, Gibbet Hill Road, Coventry, CV4 7AL, United Kingdom.*

[‡]*Center for Computational Energy Research, Department of Applied Physics, Eindhoven University of Technology, P.O. Box 513, 5600MB, Eindhoven, The Netherlands.*

[¶]*University of Warwick, Department of Chemistry, Gibbet Hill Road, Coventry, CV4 7AL, United Kingdom.*

E-mail: j.lloyd-hughes@warwick.ac.uk

Phone: +44 2476 522 043

Abstract

The dynamic increase in THz photoconductivity resulting from energetic intraband relaxation was used to track the formation of highly mobile charges in thin films of the tin iodide perovskite $Cs_{1-x}Rb_xSnI_3$, with $x = 0$ and $x = 0.1$. Energy relaxation times were found to be around 500 fs, comparable to those in the prototypical inorganic semiconductor GaAs. At low excess energies the efficient intraband energy relaxation in the lowest conduction and valence bands of $Cs_{1-x}Rb_xSnI_3$ can be understood within the context of the Fröhlich electron-phonon interaction, with a strong coupling strength. For higher excess energies the photoconductivity rise time lengthens in accordance with carrier injection into multiple bands, identified by quantitative first-principles band-structure calculations and photoluminescence spectroscopy. The findings contribute to the development of design rules for photovoltaic devices capable of extracting hot carriers from perovskite semiconductors.

Introduction

The rapid advent of metal halide perovskite semiconductors for optoelectronics has led to numerous studies of the fundamentals of light absorption, emission, and electrical transport in these novel solution-processable compounds.[1–4] The electron-phonon interaction and polaron formation are increasingly identified as controlling the electrical mobility at room temperature in the absence of extrinsic scattering mechanisms.[4–7] Recent studies using ultrafast pump-probe spectroscopies have identified intriguing hot carrier phenomena in metal halide perovskites: relatively long-lived hot carriers have been observed at high fluences and for excitation well above the bandgap.[8–11] These hot carriers can undergo long-range transport,[12] suggesting the possibility of harvesting hot-carriers in a photovoltaic device and beating the Shockley-Queisser limit. Cooling rates vary widely and depend on the material, pump energy and fluence, and yield hot carriers that persist for ∼1 ps,[8,13] ∼10 ps,[9] or over 100 ps.[10,14,15] Various contributions to hot-carrier cooling have been identified, in-

cluding a hot-phonon bottleneck,[9] Auger heating,[13] the low thermal conductivity found in organic-inorganic perovskites,[16] the possible role of higher conduction bands[16] and liquid-like reorientations of organic cations.[14] This recent work underscores the need to better understand the non-equilibrium carrier dynamics of hot electrons and holes in metal halide perovskites, in particular during intraband energy relaxation processes, in order to control hot carrier relaxation times.

Optical pump, THz probe spectroscopy (OPTP) has provided detailed insights into the mobility and recombination kinetics of metal halide perovskites, principally on organic methylammonium (MA) and formadinium (FA) lead and tin compounds.[17–22] Here, the total photoconductivity of photoexcited electrons and holes, $\Delta\sigma(t)$ at pump-probe delay t, is linked to the measured differential THz transmission $\Delta E/E$.[23] The decay dynamics of $\Delta\sigma$ on timescales $10\,\mathrm{ps} < t < 3\,\mathrm{ns}$ can be used to determine the monomolecular, bimolecular and Auger recombination rates.[20,22] On earlier timescales OPTP with band-edge excitation has been used to probe free carrier formation in methylammonium lead iodide single crystals, which form within 1 ps.[19] A less common use of OPTP is to study hot carrier relaxation within a band, on timescales below 10 ps. While transient absorption and photoluminescence spectroscopies provide information about carrier populations and temperatures, they do not directly probe the carrier conductivity. A large excess carrier energy produces a small initial $\Delta\sigma$, owing to the higher carrier effective masses away from band extrema. OPTP then tracks carrier relaxation to lower mass states by observing the time taken for the photoconductivity to increase during intraband energetic relaxation, as previously reported for the III-V semiconductors GaAs,[24,25] InGaAs[26] and InAs.[27]

Inorganic tin halide perovskites are emerging as a promising materials class for optoelectronic applications, as exemplified by B-γ phase $CsSnI_3$, which offers strong interband absorption and photoluminescence, a high electron and hole mobility, and potential use in photovoltaics.[28–31] One challenge is that tin vacancies can readily form,[32–34] leading to heavily p-type semiconductors ($10^{17} - 10^{19}\,\mathrm{cm}^{-3}$ acceptor densities), which can be regarded

as metallic[32] in the degenerately doped limit ($10^{19}\,\mathrm{cm}^{-3}$). The tin vacancy density can be minimized by the presence of excess tin halide during film deposition,[29,35] offering semiconducting behavior and improved solar cell characteristics.[29,36,37] Thin-film samples with 10 % excess SnI_2 can produce material with a low ($<10^{18}\,\mathrm{cm}^{-3}$) equilibrium hole density.[36] Cation-tuning of the electronic bandstructure has been suggested as a route to improved performance of all-inorganic tin perovskites:[38] here a small Rb fraction ($x \leq 0.1$) was used, which was recently found to increase the open-circuit voltage of model inverted photovoltaic cells.[37]

In this Article we report a study of the energy relaxation of hot carriers in the tin halide perovskite $Cs_{1-x}Rb_xSnI_3$ ($x \leq 0.1$). Partial Rb substitution was adopted as it benefits PV performance.[37] In addition to the importance of this material for PV applications, it is also a cleaner model system to study hot carrier cooling effects than the organic-inorganic lead halide perovskites for two reasons. Firstly, the choice of an inorganic A-site cation (Cs/Rb) eliminates possible effects associated with reorientations of the organic cations.[14] Secondly, tin perovskites have lower Auger recombination rates than their lead counterparts:[21] in lead perovskites, the three-particle Auger effect increases the energy of the carrier that does not recombine, helping maintain elevated temperatures.[13] Experimental results from OPTP, with variable pump wavelengths between the bandgap and the peak of the solar spectrum, were used to determine energy relaxation times over the range most relevant for photovoltaic applications. We interpret the findings using complementary results from photoluminescence spectroscopy, bandstructure calculations and a model of the electron-LO phonon energy loss rate.

Methods

Materials

CsI (Sigma-Aldrich 99.9%), SnI_2 (Alfa Aesar, 99.999%), $SnCl_2$ (Sigma Aldrich, 99.99%), RbI (Sigma-Aldrich 99.9%), N,N-dimethylformamide (DMF) (Fischer Scientific, extra dry, 99.8%).

Perovskite film synthesis

In a dry nitrogen filled glovebox (<1 ppm O_2 and <1 ppm H_2O) CsI, RbI, SnI_2 and tin(II) halide were mixed together in $(1-x):x:1:0.1$ molar ratio, where $x = 0$ or 0.1. To this mixture DMF was added to make solutions with 8, 16 and 20 wt% (total mass of solids), which were stirred overnight before use. To deposit films a few drops of a particular wt% solution were dropped on to the substrate to cover the entire surface, followed by spinning at 4000 rpm for 30 seconds. Film thicknesses were 50 nm (8 wt%), 80 nm (at 16 wt%) or 100 nm (20 wt%). The B-γ phase forms immediately upon solvent evaporation, as confirmed by X-ray diffraction, UV-visible absorption and photoluminescence measurement. The substrate used was z-cut quartz, and samples were then either encapsulated with a top layer of PMMA, or a second z-cut quartz substrate, which was sealed by an epoxy while inside the glove box. The choice of substrate ensured excellent transparency across the UV, visible and THz. The optical colour of the films (dark brown) and the band-edge photoluminescence were monitored to ensure that encapsulated films did not oxidise into Y-$CsSnI_3$ or Cs_2SnI_6 during this study. An undoped single crystal of (100)-orientation was used for the measurements on GaAs.

Terahertz spectroscopy

An optical-pump, THz-probe spectrometer based on an ultrafast Ti:sapphire amplifier (Newport Spectra Physics Spitfire Ace, 13 mJ, 1kHz, 40 fs) was used. An optical parametric ampli-

fier (TOPAS Prime, Light Conversion), pumped by 3 mJ of the amplifier's beam, generated tunable 50 fs-duration pump pulses in the visible range from 470 nm to 790 nm. The THz probe was generated by optical rectification in GaP, and detected by electro-optic sampling in ZnTe using a balanced photodiode scheme and a high-precision, high-resolution oscilloscope (Pico Technology PicoScope 4262) for data acquisition. A 4-pulse scheme, with the THz beam chopped at 500 Hz, and the optical pump chopped at 250 Hz, provided the transmitted THz electric field amplitudes E_{off} and E_{on}, and $\Delta E/E = (E_{\text{on}} - E_{\text{off}})/E_{\text{off}}$. The THz and optical pump beam diameters were measured by the knife-edge method, and yielded a Gaussian profile with standard deviation 300 μm for the THz beam and 1.2 mm for the optical pump beam. The optical pump beam was realigned after each wavelength change by maximising $\Delta E/E$ on the GaAs reference sample. The THz generation and detection beams (800 nm) were delayed relative to the fixed optical pump beam using a gold-retroreflector mounted on a motorised stage, creating a 3 ns delay line.

Photoluminescence spectroscopy

Commercial micro-Raman spectrometers (Renishaw inVia) were used to obtain photoluminescence spectra at multiple points across the $Cs_{1-x}Rb_xSnI_3$ films. Excitation powers below 15 μW were used, along with a 50x long working length objective lens. No Raman active modes were observable for $CsSnI_3$ in the range from 50 cm^{-1}-1500 cm^{-1}. A temperature stage (Linkam THMS600) with liquid nitrogen cooling was used for the temperature-dependent PL measurements.

Density functional theory

The structural optimization of the B-γ orthorhombic phase of $CsSnI_3$ and $Cs_{0.25}Rb_{0.75}SnI_3$ using unit cells of 20 atoms was performed using DFT within the local density approximation (LDA)[50] implemented in the Vienna ab-initio simulation package (VASP).[51] The outermost s, p, and d (in the case of Sn) electrons are treated as valence electrons whose interactions

with the remaining ions is modeled by pseudopotentials generated within the projector-augmented wave (PAW) method.[52] An energy cutoff of 500 eV and 8× 6×8 k-point meshes were used to achieve energy and force convergence of 0.1 meV and 2 meV/Å, respectively. DFT-LDA optimized lattice parameters of $CsSnI_3$ (a = 8.649 Å, b = 12.073 Å, c = 8.190 Å) are about 3% smaller than experiments,[37] leading to underestimation of band gaps by about 250 meV. To mitigate this underestimation, in the subsequent bandstructure calculations the LDA optimized lattice parameters were expanded by 3%. This procedure keeps the ab-initio aspects of our approach without compromising accuracy. The bandstructure calculations were performed using the accurate and efficient DFT-1/2 method[39,40] taking into account the spin orbit coupling effect. The predicted bandgap of $Cs_{1-x}Rb_xSnI_3$ is in excellent agreement with experiment.[37] A denser k-point mesh of $16 \times 12 \times 16$ was used to obtain high quality bandstructures with details shown in Figure 1 and Table 1 and discussed in the main text.

Results

Density functional theory

To identify the relevant excitation wavelengths for hot carrier excitation in $Cs_{1-x}Rb_xSnI_3$, we first examined the bandstructure of $Cs_{1-x}Rb_xSnI_3$ using the DFT-1/2 method, taking into account the spin orbit coupling effect,[39] which enables accurate bandgap predictions by introducing a half-electron and half-hole, at the same computational expense as standard DFT.[40] The DFT-1/2 bandstructure within the first Brillouin zone is shown in Figure 1 for the B-γ orthorhombic phase of $CsSnI_3$. As reported previously, the valence bands derive from a mixture of Sn 5s and I 5p orbitals, while the conduction bands are predominantly Sn 5p in character.[38] The similarity between the x and z directions ($a \simeq c$) yields band dispersions that are comparable towards X and Z (black solid and dashed lines, right-hand panel of Figure 1(a)). In contrast, since $b \gg a, c$ the dispersion towards Y (black solid lines, left-hand panel) is more pronounced, and the Brillouin zone boundary is at lower wavevector.

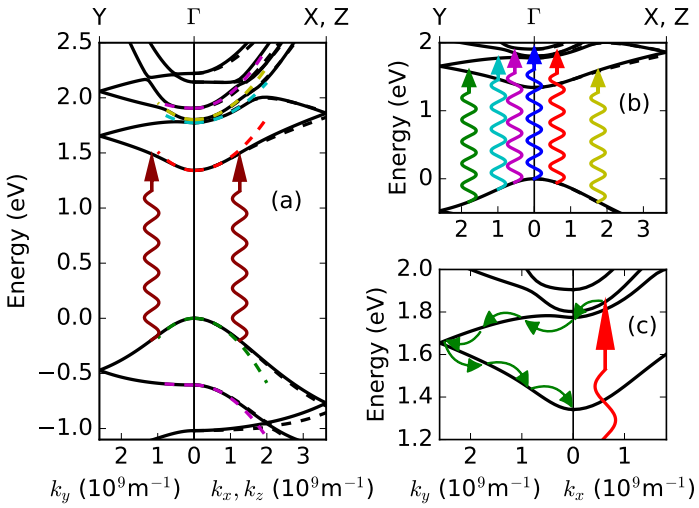

Figure 1: Bandstructure of $CsSnI_3$ calculated from the DFT-1/2 method. (a) Bands dispersion along the y-direction (left, solid black lines) and along x (right, solid black lines) and z (right, dashed black lines). Parabolic fits to the local minimum are shown by the dashed colored lines. The red arrows show interband absorption transitions at 750 nm (1.65 eV). (b) Possible interband transitions at a pump wavelength of 650 nm (1.91 eV). (c) An energy relaxation path (green arrows) within the conduction bands after 650 nm electron injection into CB3.

The dashed colored lines indicate parabolic fits to the bands close to the Γ point, yielding the effective masses reported in Table 1. Results on $Cs_{0.75}Rb_{0.25}SnI_3$ yielded comparable masses, with a slight increase in calculated bandgap energy (around 0.1 eV, Table 1) by distorting the SnI_6 octahedra.[37,38]

Photoluminescence spectroscopy

The strong absorption of B-γ $Cs_{1-x}Rb_xSnI_3$[37] can be linked to the large matrix elements for interband transitions across the Sn 5s to Sn 5p direct bandgap, such as pictured from VB1 to CB1 in Figure 1(a). In contrast, $p \rightarrow p$ transitions would have a weaker amplitude as they would not satisfy the electric dipole selection rule. After absorption, electrons (holes) relax in energy within CB1 (VB1) to the Γ point, after which they can recombine via bimolecular radiative recombination or monomolecular (trap-assisted) decay. Photoluminescence (PL) spectroscopy provides a direct probe of the energy distribution of unbound electron-hole

Table 1: Effective masses for $Cs_{1-x}Rb_xSnI_3$ at the Γ point, in units of the free-electron mass, m_e. Values for $x = 0$ and $x = 0.25$ are shown outside and inside the brackets, respectively.

Band	Energy at Γ (eV)	m_x^*, m_z^* (m_e)	m_y^* (m_e)
CB4	1.905 (2.024)	0.28 (0.28)	0.7 (0.7)
CB3	1.802 (1.887)	0.32 (0.25)	0.25 (0.32)
CB2	1.774 (1.856)	0.42 (0.5)	0.35 (0.43)
CB1	1.341 (1.445)	0.32 (0.31)	0.23 (0.24)
VB1	0.0 (0.0)	-0.26 (-0.35)	-0.21 (-0.26)
VB2	-0.605 (-0.589)	-0.32 (-0.45)	2.4 (2.2)

pairs during radiative recombination. The PL spectrum for $CsSnI_3$ under 785 nm excitation (1.58 eV) from VB1 to CB1 is reported in Figure 2(a) [red dots], with an excellent agreement between bandgap from experiment (1.349 eV) and DFT-1/2 (1.351 eV). Comparable results were obtained for $Cs_{0.9}Rb_{0.1}SnI_3$ films, with a marginal increase in bandgap with increasing x.[37] The spectrum exhibits the asymmetric shape typical of PL from non-equilibrium carriers in direct-gap semiconductors, with a high-energy tail that has a shallower gradient than the low-energy tail. Under 532 nm excitation (2.33 eV) interband absorption from VB1 can populate the first six CBs, and VB2→CB1 also becomes energetically allowed. The observed PL emission (green dots) then contains an additional peak at 1.75 eV, consistent with CB2→VB1 or CB3→VB1 transitions (Table 1).

To model the PL emission spectra we used the following expression for interband emission intensity $I(E)$ from hot carriers in a direct-gap semiconductor:

$$I(E) = I_0 e^{-(E-E_g)^2/2\sigma^2} \circledast f(E) \tag{1}$$

where $f(E) = (E - E_g)^{1/2} e^{-(E-E_g)/k_B T_e}$ for $E - E_g \geq 0$ and $f(E) = 0$ for $E - E_g < 0$, and $\circledast$ denotes taking the convolution. We assumed a Gaussian term, with width σ, to describe the symmetric broadening caused by inhomogeneous and homogenous broadening of the interband transition. The term $f(E)$ includes the Boltzmann factor at a carrier temperature T_e, which for non-equilibrium carriers is greater than the lattice temperature. Carriers are

Table 2: Photoluminescence spectra fit parameters for $CsSnI_3$, at a lattice temperature $T = 293\,\mathbf{K}$.

Excitation wavelength	Assignment	E_g (eV)	T_e (K)	σ (eV)
785 nm	CB1→VB1	1.349±0.001	343±2	0.031±0.001
532 nm	CB1→VB1	1.357±0.001	390±3	0.037±0.001
532 nm	CB2 and/or CB3→VB1	1.784±0.001	2000±50	0.100±0.002

assumed to be free to move in three dimensions in an isotropic parabolic band (yielding the $(E - E_g)^{1/2}$ term). Two such terms given by Equation 1 were used to model the 532 nm excitation spectra.

While the use of a single temperature to model the photoexcited carriers in this multiband, anisotropic compound is clearly a first-order approximation, it yields an excellent agreement with experiment, as indicated by the dashed lines in Figure 2(a), obtained with the parameters reported in Table 2. Under 785 nm excitation the non-equilibrium carrier temperature was $T_e = 343 \pm 2\,\mathrm{K}$ at a lattice temperature $T = 293\,\mathrm{K}$, which increased to $T_e = 390 \pm 3\,\mathrm{K}$ under 532 nm excitation. The spectral PL shape was independent of photoexcitation power over 2 orders of magnitude, indicating that the elevated temperature was not due to localized heating. Further, by tracking the peak energy and FWHM, Γ, of the PL versus lattice temperature, as reported in Figure 2(b) and (c) for $x = 0$ (squares), we demonstrate that measurements at room temperature are in the B-γ phase rather than the B-β phase, which was evident above 360 K by a change in the gradients of E_g and Γ with temperature.

Optical pump, THz probe spectroscopy

The PL results indicate that carriers in $Cs_{1-x}Rb_xSnI_3$ are hot while undergoing radiative recombination, and hence spend insufficient time within the CBs or VBs to reach thermal equilibrium with the lattice before recombining. To provide experimental insight into intraband dynamics we utilized OPTP spectroscopy over a wide range of optical pump wavelengths, generated by an optical parametric amplifier. Accurate knowledge of the pump-beam diam-

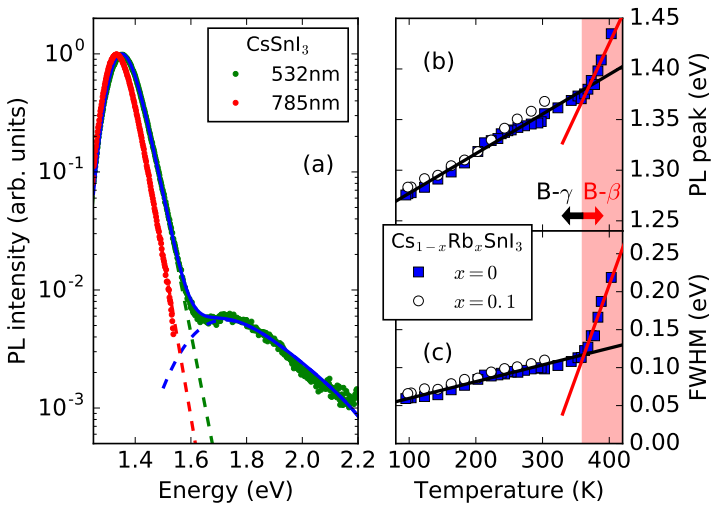

Figure 2: Photoluminescence of $CsSnI_3$ thin film encapsulated in glass. (a) PL intensity for $CsSnI_3$ at different pump wavelengths 532 nm (2.33 eV, green dots) and 785 nm (1.60 eV, red dots). Fits (dashed lines) use Equation 1. (b) PL peak for $x = 0$ (squares) and $x = 0.1$ (circles). Straight lines indicate fits to the $x = 0$ data for the B-γ phase (black line, below 360 K) and B-β phase (red line, 360 K-405 K). (c) FWHM of PL, labeled as in (b).

eter at each wavelength ensured that the same pump fluence ($\simeq 100\,\mu\mathrm{Jcm}^{-2}$) was set across the entire wavelength range. We determined the pump-induced change in the amplitude of the transmitted THz pulse, $\Delta E/E$, at early times following excitation. The photoconductivity $\Delta\sigma$ of the excited layer is proportional to -$\Delta E/E$ in the thin-film limit, which is valid for the 50 nm, 80 nm and 100 nm thick $Cs_{1-x}Rb_xSnI_3$ samples examined in this study. The absorption depth for $CsSnI_3$ was comparable to the film thickness throughout the range of wavelengths used, and hence carrier diffusion and photon reabsorption, which complicate the analysis of recombination dynamics from OPTP,[41] can be ignored. Monoexponential recombination with lifetimes from 150 ps to 300 ps were observed in all samples, ruling out bimolecular and Auger recombination at the low fluences used.

In Figure 3 the onset of photoconductivity is reported for $Cs_{0.9}Rb_{0.1}SnI_3$ and for GaAs at various photoexcitation wavelengths. In both materials the rise time for -$\Delta E/E$ to reach a maximum can be seen to increase with excess pump energy (at shorter wavelengths). For GaAs, under the lowest excess energy excitation (wavelength 780 nm) -$\Delta E/E$ increased

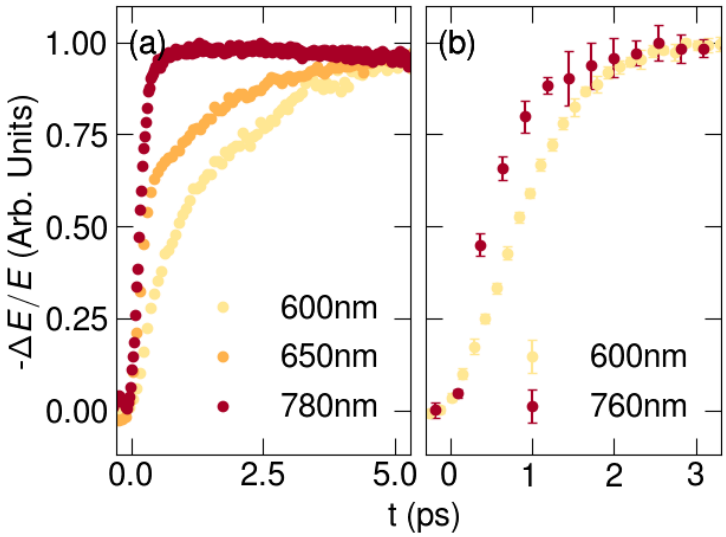

Figure 3: Photoconductivity dynamics $\Delta\sigma(t) \propto -\Delta E/E$ for (a) GaAs excited at 780 nm (red), 650 nm (orange) and 600 nm (yellow) with fluence 5 μJ/cm^2, and (b) $Cs_{0.9}Rb_{0.1}SnI_3$ excited at 760 nm (red) and 600 nm (yellow) with fluence 50 μJcm^{-2}.

rapidly within 300 fs of the pump arrival time. For GaAs the lighter electron mass in the Γ-valley than the heavy-hole mass means that the photoconductivity $\Delta\sigma = \Delta\sigma_e + \Delta\sigma_h \simeq \Delta\sigma_e$. With increasing pump energy the photoconductivity rise time increases substantially, taking around 5 ps to complete when $\lambda = 600$ nm.

To quantitatively compare the photoconductivity dynamics we performed fits of the form $\Delta E/E \propto 1 - e^{-t/\tau}$, where the photoconductivity rise time τ depends on pump wavelength λ. This analysis assumes carriers are initially injected into states with negligible photoconductivity, and then relax with time constant τ to a ground state with high mobility (low mass). The fit results, reported in Figure 4, yielded $\tau = 151$ fs at the longest pump wavelength for GaAs, which can be regarded as the shortest photoconductivity rise time observable by this spectrometer. The rise time increased marginally from an average $\tau = 155$ fs for $\lambda > 750$ nm to $\tau = 300$ fs at $\lambda = 680$ nm, due to the extra time required for electrons to cool to the Γ-valley minimum. With increasing excess energy ($\lambda < 650$ nm) the rise time increases more dramatically to $\tau > 1.5$ ps, as electrons are initially injected into high mass states (high in the conduction band), with the possibility of intervalley transfer to the high mass L- and

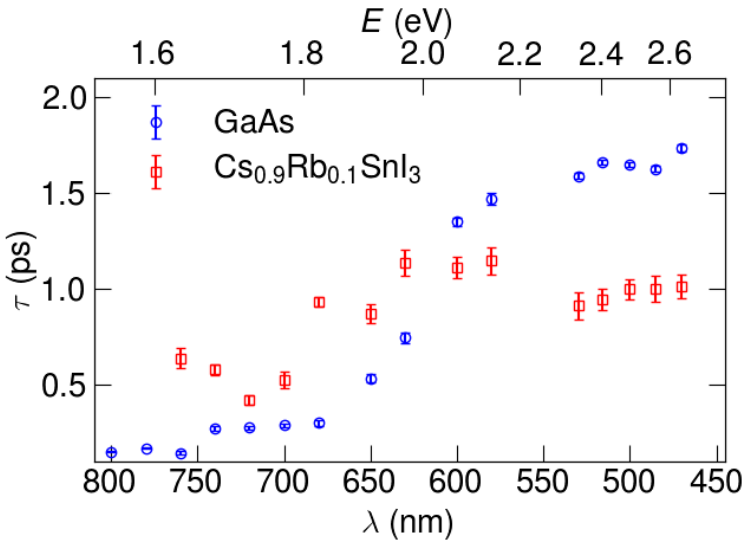

Figure 4: Photoconductivity rise time τ for $Cs_{0.9}Rb_{0.1}SnI_3$ (red squares) and GaAs (blue circles) at different optical pump wavelengths, λ.

X-valleys at photon energies above 1.71 eV and 1.90 eV, respectively.

The photoconductivity onset dynamics in $Cs_{0.9}Rb_{0.1}SnI_3$ reported in Figure 3(b) and Figure 4 display similar rise times to GaAs, but with a less substantial wavelength dependence. For $Cs_{1-x}Rb_xSnI_3$ the electron and hole masses are comparable in the different conduction and valence bands (Table 1), and hence the measured $-\Delta E/E(t) \propto \Delta\sigma_e(t) + \Delta\sigma_h(t)$ is linked to both the electron and the hole population dynamics. The measured $-\Delta E/E(t)$ rise dynamics were found to be independent of pump fluence in the range $20\,\mu\mathrm{Jcm}^{-2}$ to $200\,\mu\mathrm{Jcm}^{-2}$, and comparable rise times were obtained on $Cs_{1-x}Rb_xSnI_3$ with $x = 0$, $x = 0.1$ and $x = 0.2$.

At lower excess energies (longer wavelengths) the photoconductivity rises to a maximum within 1 ps, with an average $\tau = 0.54 \pm 0.08$ ps over the range from 760 nm to 700 nm (Figure 4). For these pump wavelengths carrier injection is into VB1 and CB1 only, as pictured schematically for 750 nm excitation in Figure 1(a). With a 650 nm pump (1.91 eV) electrons and holes are generated with higher initial masses in VB1 and CB1, and electrons can be created in CB2, CB3 and CB4, as pictured in Figure 1(b). This leads to a slower photoconductivity rise of an average $\tau = 0.90 \pm 0.3$ ps at photon energies above 1.8 eV. Above

1.95 eV VB2→CB1 is energetically allowed, and τ remains around 1.0 ps, faster than that for GaAs.

Modeled energy relaxation time

The Fröhlich treatment of the inelastic electron-LO phonon interaction, which dominates intraband energy relaxation in polar semiconductors at room temperature, can be used to model the rate of intraband energy loss.[42,43] This approach determines the net energy cooling rate from LO phonon emission and absorption, and hence the energy relaxation time τ_E. If the experimental rate $1/\tau$ is similar to $1/\tau_E$ then the Fröhlich mechanism can be regarded as the dominant cooling path, rather than other inelastic energy-loss mechanisms (such as acoustic phonon scattering). For hot carriers with a Maxwell-Boltzmann energy distribution, characterized by a temperature T_e above the lattice temperature T, τ_E can be determined from

$$\tau_E = \frac{3\sqrt{\pi}\hbar}{4k_B\alpha}\frac{\sqrt{T_e}\,(T_e - T)}{\Theta^{5/2}K_0(\Theta/2T_e)}\frac{\sinh\left(\Theta/2T\right)}{\sinh\left((T_e - T)\Theta/2TT_e\right)} \tag{2}$$

where the phonon temperature Θ is defined by $k_B\Theta = \hbar\omega_{\mathrm{LO}}$ for LO-phonon energy $\hbar\omega_{\mathrm{LO}}$ and K_0 is a modified Bessel function of the second kind.[43] The dimensionless Fröhlich electron-phonon coupling constant, α, can be determined via $\alpha = (e^2/4\pi\epsilon_0\hbar)(m^*/2\hbar\omega_{\mathrm{LO}})^{1/2}(\epsilon_\infty^{-1} - \epsilon_s^{-1})$ given knowledge of the static and high-frequency dielectric constants, ϵ_s and ϵ_∞ and the bare band mass m^*. For GaAs the electron-phonon coupling is small, with $\alpha = 0.073$ ($m^* = 0.067m_e$, $\epsilon_s = 12.95$, $\epsilon_\infty = 10.89$, $\omega_{\mathrm{LO}}/2\pi = 8.8$ THz), while for metal halide perovskites such as $CsSnI_3$ the stronger ionic bonding[44] leads to larger values of α in the range between 1 and 4. While this formalism was derived for the case of weak electron-phonon coupling,[42] it has been used to model electronic temperatures observed in transient absorption spectroscopy on $MAPbI_3$.[9,13]

To estimate α and τ_E for $CsSnI_3$ we used values ($\epsilon_s = 48$, $\epsilon_\infty = 6$) from first principles calculations,[44] given the sparcity of experimental data for the dielectric constants and phonon

frequencies. This lack is due to the large p-type doping typically found for B-γ $CsSnI_3$, which has hindered the experimental determination of the phonon modes frequencies from Raman and FTIR spectroscopy,[35] and the determination of ϵ_s. The optical phonon frequencies from first-principles calculations for the B-γ phase lie in the range from 0.5 THz and 4.0 THz, with the strongest phonon density of states between 1.0 THz and 2.0 THz.[44–46] This yields either $\alpha \simeq 3.0$ for $m^* = 0.25m_e$ and $\omega_{\mathrm{LO}}/2\pi = 2.0\,\mathrm{THz}$ (parameter set A) or $\alpha \simeq 4.2$ for $m^* = 0.25m_e$ and $\omega_{\mathrm{LO}}/2\pi = 1.0\,\mathrm{THz}$ (parameter set B), which were used to determine the energy relaxation time from Equation 2 as a function of the hot carrier temperature T_e.

The energy relaxation times calculated for $CsSnI_3$ and GaAs are reported in Figure 5 versus T_e. Also shown is the average carrier kinetic energy E_k above the band minimum, calculated from $E_k = \frac{3}{2}k_B T_e$. The above formalism, which was derived for single, spherical bands, can only be applied for low E_k, where multiple bands can be ignored. For GaAs the energy relaxation time is around 300 fs in this limit, which can be compared to the experimental 155 fs at long pump wavelengths (low E_k). The electron-LO phonon interaction thus makes up around half of the total cooling rate, with the remainder from electron-acoustic phonon scattering, as suggested by recent first-principles treatments of electron cooling in GaAs.[47]

A simple analysis of Equation 2 would predict that the $\sim 4\times$ lower LO phonon frequency of $CsSnI_3$ in comparison to GaAs should to lead to a $\sim 30\times$ higher τ_E, since $\tau_E \sim \omega_{\mathrm{LO}}^{-5/2}$ (ignoring how ω_{LO} enters into K_0 and the sinh terms), and hence that LO phonon scattering does not dominate energy relaxation. However, the calculated τ_E for $CsSnI_3$ is comparable to that for GaAs: it is slightly lower for parameter set B, while parameter set A has a similar τ_E to that of GaAs at low T_e which then diverges at higher T_e. This is a consequence of the substantially greater α for the perovskite than for GaAs, which lowers τ_E, offsetting the increase in τ_E from the lower ω_{LO}. At a kinetic energy of 150 meV (corresponding to a pump wavelength of 750 nm and $T_e = 1160\,\mathrm{K}$) the experimental $\tau \sim 0.55\,\mathrm{ps}$ is in reasonable accord with $\tau_E \sim 0.45\,\mathrm{ps}$ from parameter set A. This agreement is reasonable given the uncertainty

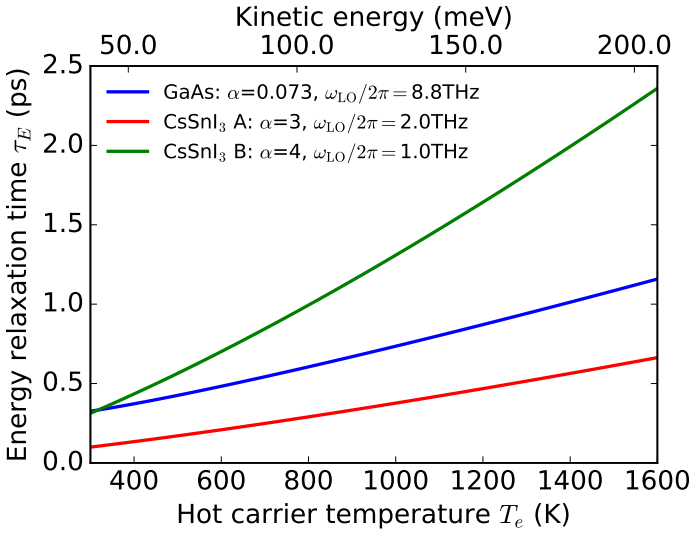

Figure 5: Energy relaxation time τ_E calculated for hot carriers at a lattice temperature $T = 300\,\mathrm{K}$ and for parameters representative of GaAs (blue curve) and $CsSnI_3$ (green and red curves).

in α and ω_{LO}.

Discussion

The good qualitative agreement between the intraband energy relaxation time in the Frölich description and the experimental τ suggests that the electron-phonon interaction may control the energetic relaxation of hot carriers in metal halide perovskites. Despite the lower LO phonon frequencies in the halide perovskites than in GaAs, the electron cooling times τ_E can be comparable as a result of the enhanced electron-phonon interaction strength, α (Equation 2). It is important to note that the calculated results for τ_E are valid in the low excess energy limit, where bands can be approximated as parabolic, and for the single band case only. More realistic models of energy relaxation need to include acoustic phonon scattering, excitonic effects and the inherent anisotropy of the bandstructure (Figure 1), the phonon dispersion, and α. For instance, a possible electron relaxation pathway after photoexcitation at 650 nm is shown by the green arrows in Figure 1(c). Interband scattering from CB3 to CB2 should

be fast close to the Γ point, for instance as energetic disorder in real materials will likely make these bands degenerate. From the Γ-point, electrons in CB2 cannot relax in energy by phonon emission along x or z, although relaxation through CB2 and CB1 associated with momentum changes in y is possible. Such anisotropic processes cannot be distinguished with the existing experiments on thin films with randomly oriented grains but should be considered in a complete theoretical treatment.

Conclusion

The hot carrier relaxation dynamics in the tin halide perovskite $Cs_{1-x}Rb_xSnI_3$ was shown to be consistent with the energy loss mediated by the electron-LO phonon interaction, by the combination of wavelength-dependent THz photoconductivity dynamics, photoluminescence spectroscopy, and first principle calculations. Energy relaxation was found to proceed on timescales similar to those in GaAs over the range of pump wavelengths and fluences relevant to perovskite solar cells. Such a fast and efficient energy relaxation is surprising given the lower LO phonon energy of the perovskites studied, and points to an enhanced electron-phonon coupling strength. These energy relaxation times imply that designs for tin-based perovskite photovoltaics that are capable of efficiently extracting hot carriers must necessarily include rapid charge extraction from the perovskite, within 1 ps. This is routinely achieved at interfaces in organic semiconductors[48] and in dye-sensitised solar cells.[49]

Acknowledgements

The authors would like to thank the EPSRC (UK) for funding part of this work. S. X. Tao acknowledges funding by the Computational Sciences for Energy Research (CSER) tenure track program of Shell, NWO, and FOM (Project number 15CST04-2).

References

(1) Zhang, W.; Eperon, G. E.; Snaith, H. J. Metal halide perovskites for energy applications. *Nature Energy* **2016**, *1*, 16048.

(2) Sutherland, B. R.; Sargent, E. H. Perovskite photonic sources. *Nature Photonics* **2016**, *10*, 295–302.

(3) Huang, J.; Yuan, Y.; Shao, Y.; Yan, Y. Understanding the physical properties of hybrid perovskites for photovoltaic applications. *Nature Reviews Materials* **2017**, *2*, 17042.

(4) Herz, L. M. Charge-carrier mobilities in metal halide perovskites: fundamental mechanisms and limits. *ACS Energy Letters* **2017**, *2*, 1539–1548.

(5) Zhu, X.-Y.; Podzorov, V. Charge carriers in hybrid organic-inorganic lead halide perovskites might be protected as large polarons. *The Journal of Physical Chemistry Letters* **2015**, *6*, 4758–4761.

(6) Wright, A. D.; Verdi, C.; Milot, R. L.; Eperon, G. E.; Pérez-Osorio, M. A.; Snaith, H. J.; Giustino, F.; Johnston, M. B.; Herz, L. M. Electron-phonon coupling in hybrid lead halide perovskites. *Nature Communications* **2016**, *7*, 11755.

(7) Miyata, K.; Meggiolaro, D.; Trinh, M. T.; Joshi, P. P.; Mosconi, E.; Jones, S. C.; De Angelis, F.; Zhu, X.-Y. Large polarons in lead halide perovskites. *Science Advances* **2017**, *3*, e1701217.

(8) Price, M. B.; Butkus, J.; Jellicoe, T. C.; Sadhanala, A.; Briane, A.; Halpert, J. E.; Broch, K.; Hodgkiss, J. M.; Friend, R. H.; Deschler, F. Hot-carrier cooling and photoinduced refractive index changes in organic-inorganic lead halide perovskites. *Nature Communications* **2015**, *6*, 8420.

(9) Yang, Y.; Ostrowski, D. P.; France, R. M.; Zhu, K.; Van De Lagemaat, J.; Luther, J. M.;

Beard, M. C. Observation of a hot-phonon bottleneck in lead-iodide perovskites. *Nature Photonics* **2016**, *10*, 53–59.

(10) Bretschneider, S. A.; Laquai, F.; Bonn, M. Trap-free hot carrier relaxation in lead-halide perovskite films. *Journal of Physical Chemistry C* **2017**, *121*, 11201–11206.

(11) Fang, H. H.; Adjokatse, S.; Shao, S.; Even, J.; Loi, M. A. Long-lived hot-carrier light emission and large blue shift in formamidinium tin triiodide perovskites. *Nature Communications* **2018**, *9*, 243.

(12) Guo, Z.; Wan, Y.; Yang, M.; Snaider, J.; Zhu, K.; Huang, L. Long-range hot-carrier transport in hybrid perovskites visualized by ultrafast microscopy. *Science* **2017**, *356*, 59–62.

(13) Fu, J.; Xu, Q.; Han, G.; Wu, B.; Huan, C. H. A.; Leek, M. L.; Sum, T. C. Hot carrier cooling mechanisms in halide perovskites. *Nature Communications* **2017**, *8*, 1300.

(14) Zhu, H.; Miyata, K.; Fu, Y.; Wang, J.; Joshi, P. P.; Niesner, D.; Williams, K. W.; Jin, S.; Zhu, X.-Y. Screening in crystalline liquids protects energetic carriers in hybrid perovskites. *Science (New York, N.Y.)* **2016**, *353*, 1409–1413.

(15) Niesner, D.; Zhu, H.; Miyata, K.; Joshi, P. P.; Evans, T. J. S.; Kudisch, B. J.; Trinh, M. T.; Marks, M.; Zhu, X.-Y. Persistent energetic electrons in methylammonium lead iodide perovskite thin films. *Journal of the American Chemical Society* **2016**, *138*, 15717–15726.

(16) Frost, J. M.; Whalley, L. D.; Walsh, A. Slow cooling of hot polarons in halide perovskite solar cells. *ACS Energy Letters* **2017**, *2*, 2647–2652.

(17) Wehrenfennig, C.; Eperon, G. E.; Johnston, M. B.; Snaith, H. J.; Herz, L. M. High charge carrier mobilities and lifetimes in organolead trihalide perovskites. *Adv. Mater.* **2014**, *26*, 1584–1589.

(18) La-o vorakiat, C.; Salim, T.; Kadro, J.; Khuc, M.-T.; Haselsberger, R.; Cheng, L.; Xia, H.; Gurzadyan, G. G.; Su, H.; Lam, Y. M. et al. Elucidating the role of disorder and free-carrier recombination kinetics in $CH_3NH_3PbI_3$ perovskite films. *Nature Communications* **2015**, *6*, 7903.

(19) Valverde-Chávez, D. A.; Ponseca, C. S.; Stoumpos, C. C.; Yartsev, A.; Kanatzidis, M. G.; Sundström, V.; Cooke, D. G. Intrinsic femtosecond charge generation dynamics in single crystal $CH_3NH_3PbI_3$. *Energy Environ. Sci.* **2015**, *8*, 3700–3707.

(20) Milot, R. L.; Eperon, G. E.; Snaith, H. J.; Johnston, M. B.; Herz, L. M. Temperature-dependent charge-carrier dynamics in $CH_3NH_3PbI_3$ perovskite thin films. *Advanced Functional Materials* **2015**, *25*, 6218–6227.

(21) Milot, R. L.; Eperon, G. E.; Green, T.; Snaith, H. J.; Johnston, M. B.; Herz, L. M. Radiative monomolecular recombination boosts amplified spontaneous emission in $HC(NH_2)_2SnI_3$ perovskite films. *The Journal of Physical Chemistry Letters* **2016**, *7*, 4178–4184.

(22) Johnston, M. B.; Herz, L. M. Hybrid perovskites for photovoltaics: charge-carrier recombination, diffusion, and radiative efficiencies. *Accounts of Chemical Research* **2016**, *49*, 146–154.

(23) Joyce, H. J.; Boland, J. L.; Davies, C. L.; Baig, S. A.; Johnston, M. B. A review of the electrical properties of semiconductor nanowires: insights gained from terahertz conductivity spectroscopy. *Semiconductor Science and Technology* **2016**, *31*, 103003.

(24) Nuss, M. C.; Auston, D. H.; Capasso, F. Direct subpicosecond measurement of carrier mobility of photoexcited electrons in gallium-arsenide. *Phys. Rev. Lett.* **1987**, *58*, 2355–2358.

(25) Beard, M. C.; Turner, G. M.; Schmuttenmaer, C. A. Transient photoconductivity in

GaAs as measured by time-resolved terahertz spectroscopy. *Phys. Rev. B* **2000**, *62*, 15764–15777.

(26) Ralph, S. E.; Chen, Y.; Woodall, J.; McInturff, D. Subpicosecond photoconductivity of $In_{0.53}Ga_{0.47}As$: intervalley scattering rates observed via THz spectroscopy. *Phys. Rev. B* **1996**, *54*, 5568–5573.

(27) Lloyd-Hughes, J. Generalized conductivity model for polar semiconductors at terahertz frequencies. *Applied Physics Letters* **2012**, *100*, 122103.

(28) Shum, K.; Chen, Z.; Qureshi, J.; Yu, C.; Wang, J. J.; Pfenninger, W.; Vockic, N.; Midgley, J.; Kenney, J. T. Synthesis and characterization of $CsSnI_3$ thin films. *Applied Physics Letters* **2010**, *96*, 221903.

(29) Marshall, K. P.; Walker, M.; Walton, R. I.; Hatton, R. A. Enhanced stability and efficiency in hole-transport-layer-free $CsSnI_3$ perovskite photovoltaics. *Nature Energy* **2016**, *1*, 16178.

(30) Wang, N.; Zhou, Y.; Ju, M.-G.; Garces, H. F.; Ding, T.; Pang, S.; Zeng, X. C.; Padture, N. P.; Sun, X. W. Heterojunction-depleted lead-free perovskite solar cells with coarse-grained B-γ-$CsSnI_3$ thin films. *Advanced Energy Materials* **2016**, *6*, 1601130.

(31) Wu, B.; Zhou, Y.; Xing, G.; Xu, Q.; Garces, H. F.; Solanki, A.; Goh, T. W.; Padture, N. P.; Sum, T. C. Long minority-carrier diffusion length and low surface-recombination velocity in inorganic lead-free $CsSnI_3$ perovskite crystal for solar cells. *Advanced Functional Materials* **2017**, *27*, 1604818.

(32) Chung, I.; Song, J.-H. H.; Im, J.; Androulakis, J.; Malliakas, C. D.; Li, H.; Freeman, A. J.; Kenney, J. T.; Kanatzidis, M. G. $CsSnI_3$: semiconductor or metal? High electrical conductivity and strong near-infrared photoluminescence from a single material. High hole mobility and phase-transitions. *J. Am. Chem. Soc.* **2012**, *134*, 8579–8587.

(33) Xu, P.; Chen, S.; Xiang, H.-J.; Gong, X.-G.; Wei, S.-H. Influence of defects and synthesis conditions on the photovoltaic performance of perovskite semiconductor $CsSnI_3$. *Chemistry of Materials* **2014**, *26*, 6068–6072.

(34) Rajendra Kumar, G.; Kim, H.-J.; Karupannan, S.; Prabakar, K. Interplay between iodide and tin vacancies in $CsSnI_3$ perovskite solar cells. *The Journal of Physical Chemistry C* **2017**, *121*, 16447–16453.

(35) Kontos, A. G.; Kaltzoglou, A.; Siranidi, E.; Palles, D.; Angeli, G. K.; Arfanis, M. K.; Psycharis, V.; Raptis, Y. S.; Kamitsos, E. I.; Trikalitis, P. N. et al. Structural stability, vibrational properties, and photoluminescence in $CsSnI_3$ perovskite upon the addition of SnF_2. *Inorganic Chemistry* **2017**, *56*, 84–91.

(36) Marshall, K. P.; Walker, M.; Walton, R. I.; Hatton, R. A. Elucidating the role of the hole-extracting electrode on the stability and efficiency of inverted $CsSnI_3/C_{60}$ perovskite photovoltaics. *J. Mater. Chem. A* **2017**, *5*, 21836–21845.

(37) Marshall, K. P.; Tao, S. X.; Walker, M.; Cook, D. S.; Lloyd-Hughes, J.; Varagnolo, S.; Wijesekara, A.; Walker, D.; Walton, R. I.; Hatton, R. A. $Cs_{1-x}Rb_xSnI_3$ light harvesting semiconductors for pervoskite photovoltaics. *Materials Chemistry Frontiers* **2018**, *2*, 1515–1522.

(38) Jung, Y.-K.; Lee, J.-H.; Walsh, A.; Soon, A. Influence of Rb/Cs cation-exchange on inorganic Sn halide perovskites: from chemical structure to physical properties. *Chemistry of Materials* **2017**, *29*, 3181–3188.

(39) Ferreira, L. G.; Marques, M.; Teles, L. K. Approximation to density functional theory for the calculation of band gaps of semiconductors. *Physical Review B* **2008**, *78*, 125116.

(40) Tao, S. X.; Cao, X.; Bobbert, P. A. Accurate and efficient band gap predictions of metal halide perovskites using the DFT-1/2 method: GW accuracy with DFT expense. *Scientific Reports* **2017**, *7*, 14386.

(41) Crothers, T. W.; Milot, R. L.; Patel, J. B.; Parrott, E. S.; Schlipf, J.; Müller-Buschbaum, P.; Johnston, M. B.; Herz, L. M. Photon reabsorption masks intrinsic bimolecular charge-carrier recombination in $CH_3NH_3PbI_3$ perovskite. *Nano Letters* **2017**, *17*, 5782–5789.

(42) Conwell, E. M. Rate of energy loss to polar modes. *Physical Review* **1966**, *143*, 657–658.

(43) Seeger, K. *Semiconductor physics: an introduction*, 9th ed.; Springer Berlin Heidelberg, 2004; pp 205–209.

(44) Huang, L.-y.; Lambrecht, W. R. L. Lattice dynamics in perovskite halides $CsSnX_3$ with X = I, Br, Cl. *Physical Review B* **2014**, *90*, 195201.

(45) Patrick, C. E.; Jacobsen, K. W.; Thygesen, K. S. Anharmonic stabilization and band gap renormalization in the perovskite $CsSnI_3$. *Physical Review B* **2015**, *92*, 201205.

(46) da Silva, E. L.; Skelton, J. M.; Parker, S. C.; Walsh, A. Phase stability and transformations in the halide perovskite $CsSnI_3$. *Physical Review B* **2015**, *91*, 144107.

(47) Bernardi, M.; Vigil-Fowler, D.; Ong, C. S.; Neaton, J. B.; Louie, S. G. Ab initio study of hot electrons in GaAs. *Proceedings of the National Academy of Sciences of the United States of America* **2015**, *112*, 5291–5296.

(48) Jakowetz, A. C.; Böhm, M. L.; Zhang, J.; Sadhanala, A.; Huettner, S.; Bakulin, A. A.; Rao, A.; Friend, R. H. What controls the rate of ultrafast charge transfer and charge separation efficiency in organic photovoltaic blends. *Journal of the American Chemical Society* **2016**, *138*, 11672–11679.

(49) Tiwana, P.; Docampo, P.; Johnston, M. B.; Snaith, H. J.; Herz, L. M. Electron mobility and injection dynamics in mesoporous ZnO, SnO_2, and TiO_2 films used in dye-sensitized solar cells. *ACS Nano* **2011**, *5*, 5158–5166.

(50) Kohn, W.; Sham, L. J. Self-consistent equations including exchange and correlation effects. *Phys. Rev.* **1965**, *140*, A1133–A1138.

(51) Kresse, G.; Furthmller, J. Efficiency of ab-initio total energy calculations for metals and semiconductors using a plane-wave basis set. *Computational Materials Science* **1996**, *6*, 15 – 50.

(52) Kresse, G.; Joubert, D. From ultrasoft pseudopotentials to the projector augmented-wave method. *Phys. Rev. B* **1999**, *59*, 1758–1775.

TOC Graphic: